

Development of a material model to simulate through-the-thickness transmission of vibration in the adult human skull

Sourabh Boruah, Damien L. Subit, Jeff R. Crandall, Robert S. Salzar, Barry S. Shender, Glenn Paskoff

Abstract Brain injury resulting from exposure to blast continues to be a significant problem in the military community, often leading to death or long term disability. The presence of high frequency energy content in pressure waves generated in explosive blasts necessitates understanding the transmissibility and damping characteristics of skull bone. Current finite element models (FEM) of the skull do not include material damping and therefore fail to capture the correct attenuation spectrum or rate dependency of skull bone.

Cylindrical through-the-thickness specimens of skull bone were obtained from ten adult (55 ± 10 years old) male post-mortem human surrogates. A test apparatus was developed to apply cyclic loading to potted cores at frequencies ranging from 1 to 50 kHz using a piezoelectric shaker. High bandwidth transducers were used to record accelerations and forces at the boundary. A lumped mass model was optimized to match the recorded boundary conditions.

This paper reports composite material properties of the skull as a frequency dependent complex modulus. The calculated material loss tangent was distributed in a log-normal fashion and ranged from 0.027 to 0.194 (95 % CI). A generalized Maxwell model, represented using a Prony series has been developed and the model parameters have been reported.

Keywords *generalized Maxwell model; adult human skull, rheometry, transmissibility, viscoelastic*

I. INTRODUCTION

The study of viscoelasticity of bone began in 1970s. Viscoelastic properties obtained from creep and relaxation studies for long durations [1-2] can be used to predict behavior at low frequencies and are not relevant for dynamic events. During the same time, an instrument developed for observation of torsional stress strain behavior of small specimen was used to study viscoelasticity of pure compact bone [2]. This device was refined to deliver bending stress [3]. Yet other studies looked at decay of free vibrations [4]. All these studies were limited to pure cortical bone. Moreover these studies suffered from small number of specimens tested and were capable of frequencies up to only ~ 1 kHz. Only a few researchers have attempted to characterize composite whole bone response ([5-6]). However they have used animal whole bones and are very limited in numbers.

The study of brain injury due to explosive blasts requires the understanding of the skull behavior under somewhat different circumstances. Blast pressure is known to have significant energy content at frequencies of up to 20 kHz. Therefore data at larger frequencies is required. Reference [4] provides data at this frequency range for pure cortical bone. Skull bone has a sandwich structure with two dense cortical layers interspersed by a porous cancellous layer. It may be expected to behave differently due to the presence of pores and fluids. Current Finite Element (FE) models of the human skull have a mesh resolution of ~ 5 mm, which is close to the thickness of the skull. Therefore they sometimes have only one element through the thickness. A characterization of the composite response of the three layers of the skull will therefore be very valuable. This research develops a methodology for characterization of damping properties and attempts to provide a linear viscoelastic model of skull bone which exhibits correct response under loading conditions typically seen in explosive blast events.

II. METHODS

Materials

Skull bone specimens were obtained from the calvarium of ten adult male PMHS. The subjects, representing the 50th percentile adult male, were at an average 55 years old, 178 cm high and weighed 92 kg (TABLE I). All subjects were frozen post mortem and thawed for use. They were screened for common blood-borne pathogens and for pre-existing pathology that may influence bone properties. The University of Virginia cadaver institutional review board has reviewed and approved these test procedures. Clinical Computed Tomography (CT) was done for all subjects at a resolution of 0.625 mm in order to identify potential locations of harvesting skull bone specimens.

TABLE I
PMHS ANTHROPOMETRY

Subject no.	Age	Height [cm]	Weight [kg]
1	58	188	104
2	41	180	71
3	51	173	91
4	61	175	204
5	66	178	70
6	59	173	68
7	45	191	73
8	49	175	101
9	70	173	77
10	49	175	57

Ten locations were identified on the right half of the calvarium for harvesting through-the-thickness cylindrical skull bone specimens (skull cores). These locations were distributed across the frontal bone and the parietal bone. Following thawing of the head, and removal of the scalp, these ten locations were marked on the skull surface (Fig. 1). Specimens were also harvested from symmetric points on the left half for another experiment. The harvest locations varied from skull to skull due to the presence of un-suitable anomalies and curvatures and also to avoid sutures. The locations were measured for each skull using a 2 dimensional curvilinear coordinate system with the origin at the posterior end of the zygomatic bone. Fig. 2 shows the arrangement of this coordinate system. The first dimension is rear-wards along the intersection of the skull outer surface and the Frankfort plane and the second dimension orthogonal to the first, pointed towards the vertex of the skull.



Fig. 1. Ten test specimen harvest locations marked on the right half of the skull; two locations (8 and 10) not

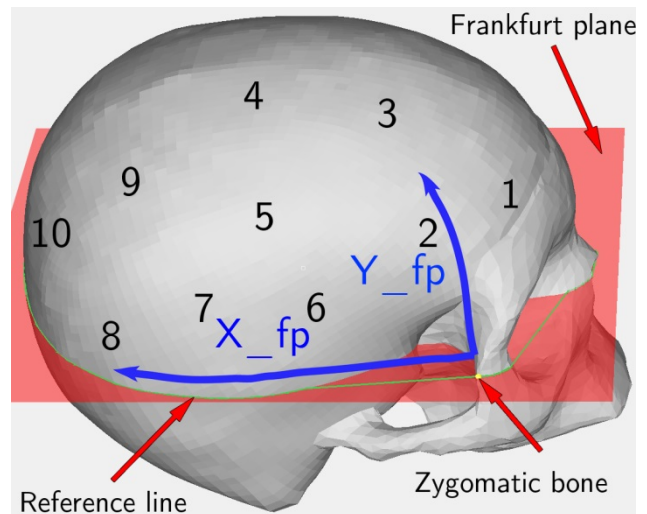


Fig. 2. The harvest locations marked on a clinical CT rendering; measurements made along the skull outer

visible.

surface relative to the zygomatic bone.

The calverium was removed using a circular oscillating saw and split into the right and left halves. Skull core specimens were then harvested using a circular abrasive drill bit on a bench drill press (Fig. 3). The bone was maintained hydrated with saline solution throughout this process to prevent excessive heating. This process yielded skull cores with a diameter of approximately 18 mm (Fig. 4).



Fig. 3. Skull cores obtained from right calverium using circular abrasive drill.

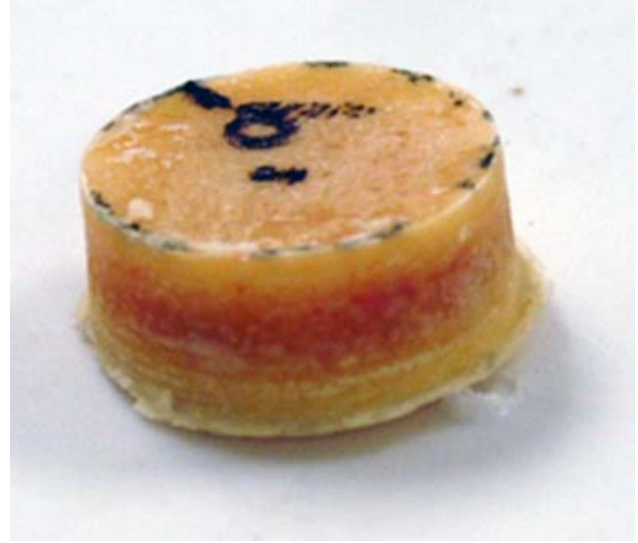


Fig. 4. A sample skull core.

Specimen Potting

The skull cores were potted in a minimal amount of polyester resin (Bondo, 3M, Maplewood, Minnesota) in order to provide two flat parallel surfaces for mounting the specimen on the test rig. The mass of the cores was measured prior to potting using an electronic scale (resolution 0.01 g). The two part filler was mixed using syringes to produce consistent potting material. It was then applied to the inner and outer tables and put in a jig to ensure flat and parallel surfaces (Fig. 5). The total potted thickness was measured using a vernier caliper.



Fig. 5. Potting of skull core in polyester using the jig device.



Fig. 6. Potted cores.

Test Setup

The transmissibility test setup (Fig. 7) consisted of a piezo-electric reaction mass type shaker (Wilcoxon F7-1) exciting the test specimen against an index table. Test instrumentation included a piezo-electric load cell (Omega DLC 101-50) and a piezo-electric accelerometer (Brüel & Kjær 8309) on both sides of the test specimen. All data was sampled at 2 MHz using a Hi-Techniques Synergy-CS data acquisition system (DAS). All the components of the test system (the shaker, instruments and test specimen) were mounted in the same horizontal axis with the core outer table facing the shaker. An index table was used to accommodate specimen of various thicknesses. The setup was installed on a vibration isolation table. A schematic of the test setup is shown in Fig. 8.

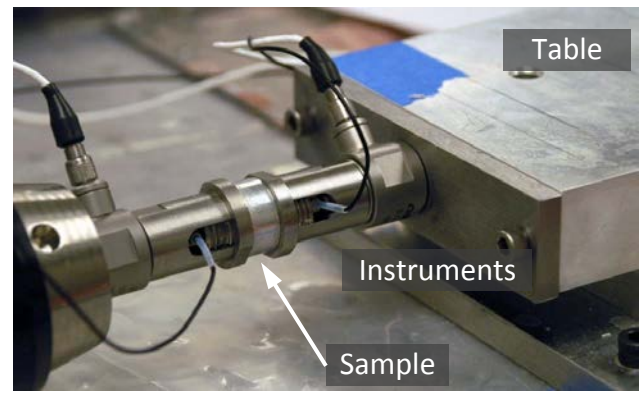
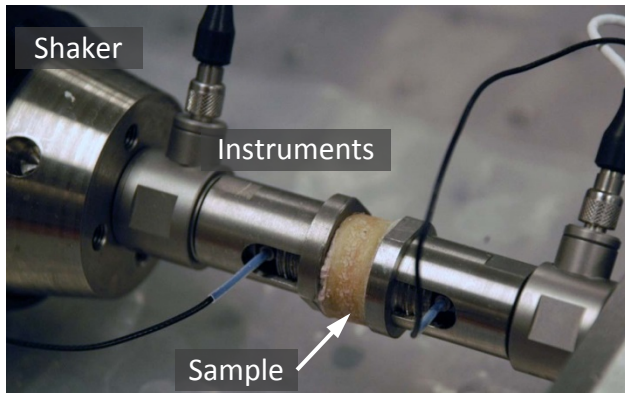


Fig. 7. Transmissibility Test setup; Shaker and shaker-side instruments (left); Index table and table-side instruments (right); please note that an aluminum placeholder sample is installed in the image on right.

The transmissibility test control system was designed and run in Labview (Fig. 9). A Rigol DG 1022 arbitrary waveform generator was controlled through USB using the National Instruments Virtual Instrument Software Architecture (NI-VISA) to calibrate the shaker power amplifier. Excitation signal amplitudes depended on the frequency of excitation and were predetermined to control oscillation near resonance spots and ensure a nearly constant displacement magnitude. There was feedback from the waveform generator confirming generation and cessation of excitation voltage. The Synergy-CS data acquisition system, controlled by Labview over the Ethernet using transmission control protocol (TCP / IP) provided feedback indicating amplitude of oscillation, which was used to ascertain steady-state vibration. The system was programmed to deliver vibration at frequencies ranging from 1 kHz to 50 kHz (evenly spaced in the logarithmic domain) and record steady state vibrations at each frequency. Frequencies at which sensor signals were saturated due to large amplitude of vibration were skipped.

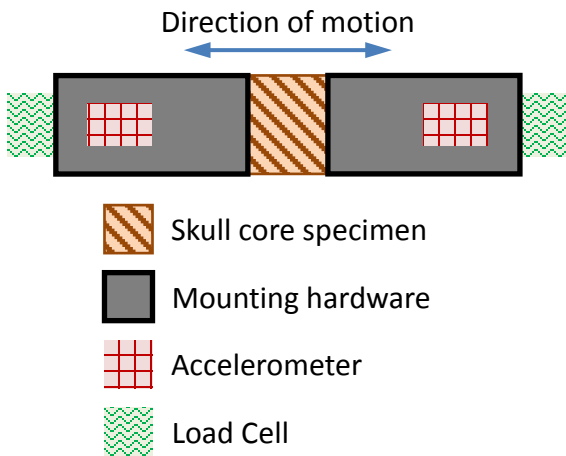


Fig. 8. Schematic of test setup; skull core specimen sandwiched between two pseudo rigid transducers consisting of mounting hardware, accelerometer and load-cell sprung mass.

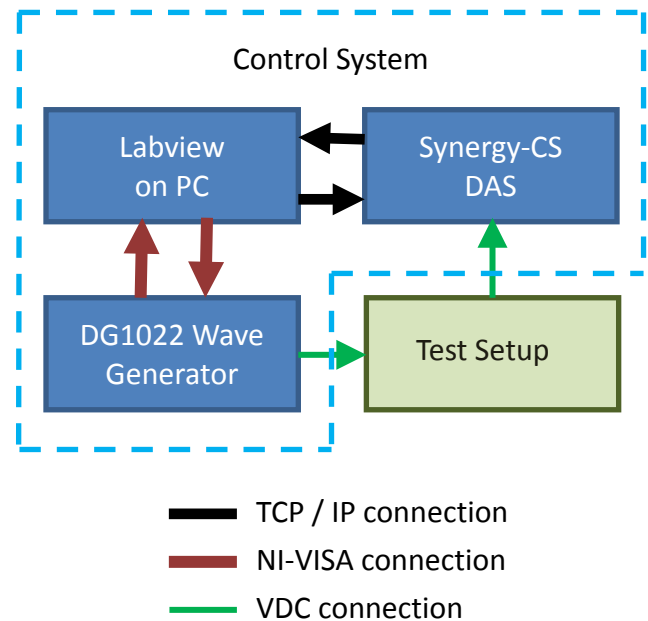


Fig. 9. Schematic of the test control system; The controller (LABVIEW software in PC) communicates via TCP / IP with data acquisition system and via NI-VISA with the waveform generator.

Theoretical Modeling – Frequency domain

This step develops an effective, one-dimensional through-the-thickness response characterization in the frequency domain. This model is non-parametric and is free of any assumptions. The core sample mass (~ 2 g) is relatively small compared to the transducers at the boundary (~ 50 g each). The presence of the relatively massive transducers precludes straightforward calculation of material response. A simple lumped mass model (free body diagram shown in Fig. 10) has been used to account for the effects of transducer inertia. The material parameter sought is calculated from the single frequency dependent complex modulus \bar{k}^* (Fig. 11). The

governing equations for this model are shown in (1). The governing equations are solved to obtain structural parameter k^* in terms of the known quantities (equation (2)).

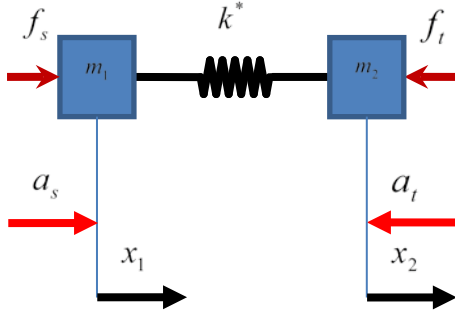


Fig. 10. Free body diagram of simple spring mass system used to model skull transmissibility in the frequency domain.

$$m_1 \ddot{x}_1 + k^*(x_1 - x_2) - f_s = 0 \quad (1)$$

$$m_2 \ddot{x}_2 + k^*(x_2 - x_1) + f_t = 0$$

$$(m_2 \ddot{x}_2 - m_1 \ddot{x}_1) + 2k^*(x_2 - x_1) + f_t + f_s = 0$$

$$k^* = \frac{(m_1 \ddot{x}_1 - m_2 \ddot{x}_2) - f_t - f_s}{2(x_2 - x_1)} \quad (2)$$

All of the variables may be expressed as a complex number in terms of their magnitudes and phases.

$$a_s = A_s^* e^{i\omega t} \Rightarrow \ddot{x}_1 = A_s^* e^{i\omega t} \Rightarrow x_1 = -\frac{A_s^* e^{i\omega t}}{\omega^2}$$

$$a_t = A_t^* e^{i\omega t} \Rightarrow \ddot{x}_2 = -A_t^* e^{i\omega t} \Rightarrow x_2 = \frac{A_t^* e^{i\omega t}}{\omega^2}$$

$$f_s = F_s^* e^{i\omega t}$$

$$f_t = F_t^* e^{i\omega t}$$

Substituting variables from equations (3) in equation (2) and cancelling $e^{i\omega t}$,

$$k^* = \frac{(m_1 A_s^* + m_2 A_t^*) - F_t^* - F_s^*}{2(A_t^* + A_s^*)} \omega^2 \quad (4)$$

The structural parameter on the left hand side of equation (4) is calculated at each frequency from the complex variables on the right hand side. Masses of the transducers (inclusive of load cell sprung mass, accelerometer and hardware) m_1 and m_1 have been measured directly. These complex variables are obtained directly from time-history data recorded during tests through discrete Fourier transform (DFT; typical magnitude spectra shown in Fig. 17). The frequency dependent structural parameter k^* is normalized by cross-section area and sample thickness to obtain the frequency dependent complex modulus E^* using relationship (5).

$$E^* = \frac{k^* l}{A} \quad \text{where, } l \text{ – Thickness of skull core sample} \quad (5)$$

A –cross-section area of sample

Theoretical Modeling – Time domain

In order to apply the frequency domain knowledge to predict response of the skull to an arbitrary event, a time domain model is needed. One of the most common models used for biomaterials is a generalized Maxwell

Transducers:

a_s or \ddot{x}_1 : Shaker side acceleration

a_t or $-\ddot{x}_2$: Table side acceleration

f_s : Shaker-side Force

f_t : Table-side Force

Lumped Masses:

m_1, m_2 : Transducer mass

Material Parameter:

k^* : Complex spring constant (frequency dependent)

Fig. 11. Glossary of frequency domain model variables and parameters.

where,

A_s^* – Shaker-side acceleration

A_t^* – Table-side acceleration

F_s^* – Shaker-side force

F_t^* – Table-side force

model (Fig. 12). The generalized Maxwell model is represented parametrically by its relaxation function (Prony series [7]). The parameters are described in Fig. 13. The Prony series was chosen since it is pre-implemented in most commercial FE solver packages and is readily applicable.

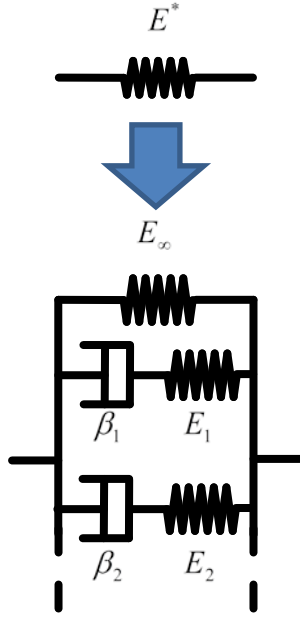


Fig. 12. Frequency dependent complex modulus converted to generalized Maxwell model.

Frequency domain material parameter:

E^* – Complex spring constant

Time domain material parameters:

E_∞ – Long term structural stiffness

E_j – Spring constant of j^{th} Maxwell element

β_j – Decay constant of j^{th} Maxwell element

Fig. 13. Glossary of time domain model parameters.

The complex modulus of the generalized Maxwell model is represented in terms of the Prony series parameters in equation (6).

$$E_{\text{max well}}^* = E_\infty + \sum_j \frac{i\omega E_j}{\beta_j + i\omega} \quad (6)$$

For simplicity of comparison, parameters β_j have been fixed and E_∞ obtained from lower rate compression tests [8]. The Maxwell unit stiffness parameters E_j are optimized to match parametric Maxwell complex modulus $E_{\text{max well}}^*$, obtained using equation (6), to frequency dependent (but non-parametric) E^* (from equation (5)) calculated from experiment data in the previous section.

III. RESULTS

A few examples of the experimental modulus and loss tangent from the experimental data are shown in Fig. 14. Although the objective was to capture data at frequencies from 1 kHz to 50 kHz, the entire spectrum could not be captured due to excessive vibration at certain frequencies and inability to attain steady-state due to the same reason. Outliers are seen typically at the higher frequency end and also at the boundaries of frequency domains of excessive vibrations (seen in all graphs in Fig. 14). The average loss tangent across the range of excitation frequencies of the 86 core samples (Fig. 15) has a median value of 0.074 (~2 to 20 kHz excitation frequency). $\tan \delta$ does not correlate with specimen or harvest location. At each frequency, the $\tan \delta$ for all cores are distributed in a log-normal fashion. Therefore to show frequency dependence, the average and confidence intervals are built in the logarithmic domain. The dependence of $\tan \delta$ on frequency and its 95 % confidence interval is shown in Fig. 16.

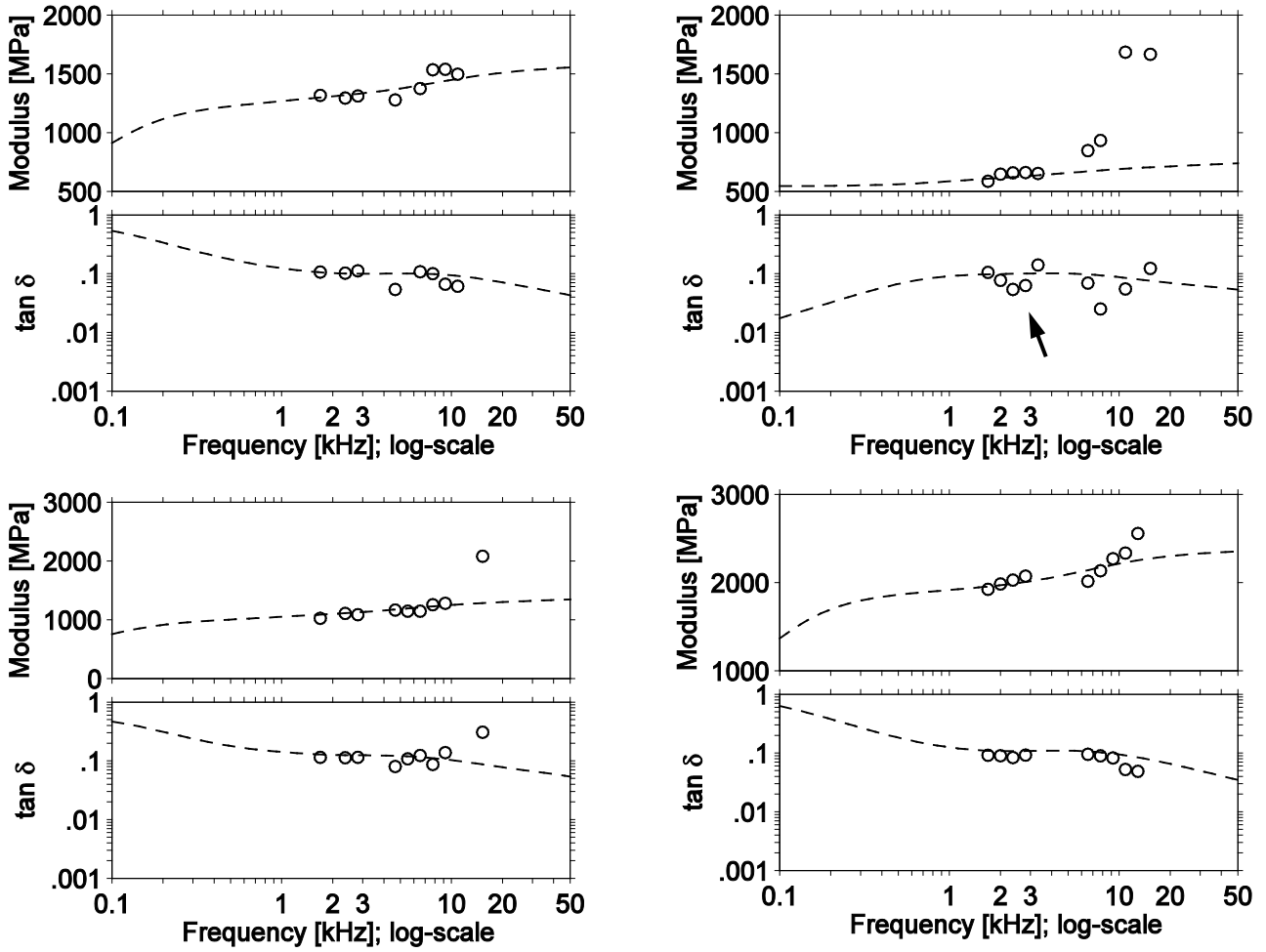


Fig. 14. Typical graphs showing change in magnitude of complex modulus (top) and loss tangent (bottom; logarithmic scale) with respect to frequency; dashed line shows a five term Prony series fit to the experimental data.

Fig. 14 also shows a five term Prony series fit to the experimental data (dashed line). The decay constants used and corresponding average stiffnesses for the 86 cores is presented in TABLE II. The Prony series function is found to be ill-suited to model experimental data that change fast with respect to frequency (arrow on top right; Fig. 14). Detailed core-wise material properties have been listed in TABLE A I. Since no tests were done below 1 kHz, all stiffness that relaxes slower than that are clubbed together in $\beta_j = 100$ Hz or 1000 Hz depending on the magnitude of loss modulus at 1000 Hz.

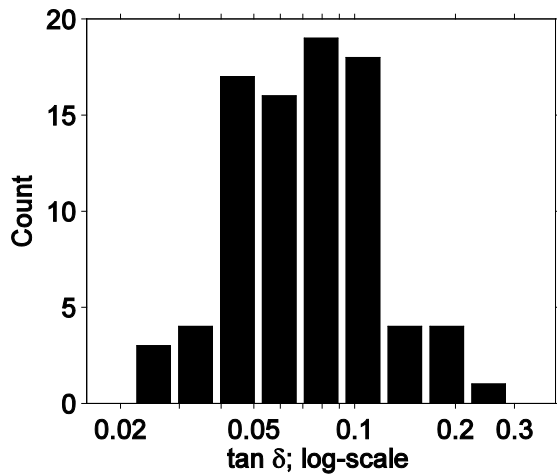


Fig. 15. Material loss tangent ($\tan \delta$) for 86 through-the-thickness skull core samples, averaged across range of excitation frequency (~ 2 to 20 kHz)

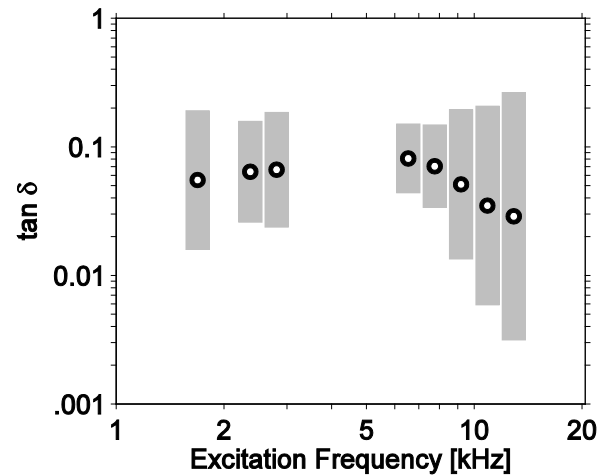


Fig. 16. Loss tangent ($\tan \delta$); expected value (circles) and 95 % confidence intervals (gray bars) at different frequencies on vibration; note: $\tan \delta$ has a log-normal

distribution.

TABLE II
PRONY SERIES GLOBAL AVERAGE

β_i [Hz]	E_i [MPa]		E [%] (of E_∞)	
	Mean	SD	Mean	SD
*0	450	144		
100	1346	585	316	148
1000	81	86	20	22
5000	132	64	31	17
10000	136	77	32	21
50000	74	75	17	15

* - taken from reference [8]

IV. DISCUSSION

Spectrum and noise

The raw data acquired in the experiments was filtered using a 10-pole linear-phase 200 kHz analog filter which provided more than 95 dB alias rejection at 1 MHz and made the data suitable for spectral analysis up to 200 kHz. Apart from this, no other filter was used on the data. Fig. 17 shows an example of the data spectra. The peaks in the magnitude spectrum always occur at the excitation frequency and the magnitude and phase of the four variables (shaker-side and table-side forces and accelerations) at this frequency are used in equation (4) to obtain the complex structural stiffness parameter at that frequency. This procedure effectively cancels out all the components of data at frequencies other than the excitation frequency and thus eliminates all the noise. The spectrum also shows significant vibration at the harmonics of excitation frequency (black arrows in Fig. 17). Although this data could be potentially used, they have not been included in this paper.

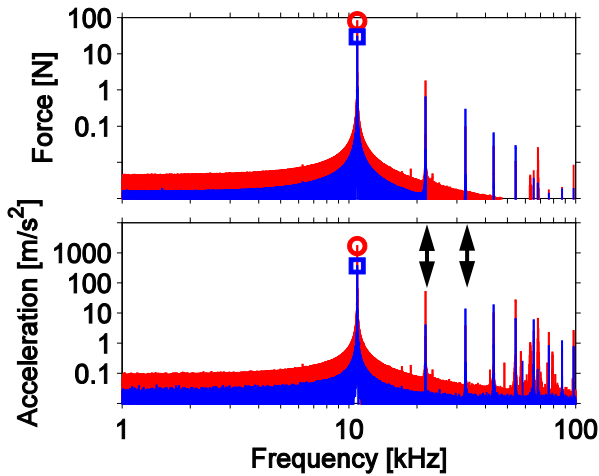


Fig. 17. Typical magnitude spectrum of forces (top) and accelerations (bottom) estimated using MATLAB DFT; red – shaker-side; blue – table-side; circle – shaker-side spectrum peak at excitation frequency; square – table-side spectrum peak at excitation frequency

Comparison to ramp compression tests

Dynamic compression tests were conducted on the same cores after transmissibility testing. This series of tests can be represented by an average compression of 0.70 ± 0.45 mm and a rise time of 139 ± 60 ms (Fig. 18). This ramp can be decomposed into sine-wave components having frequencies starting from 7.2 Hz up to ∞ with amplitude inversely proportional to frequency. The tenth component represents 3.5 % contribution to the ramp; therefore, sine-wave components having frequencies greater than ~ 70 Hz may be safely neglected. The smallest frequency (decay constant) chosen for the generalized Maxwell model was 100 Hz representing the

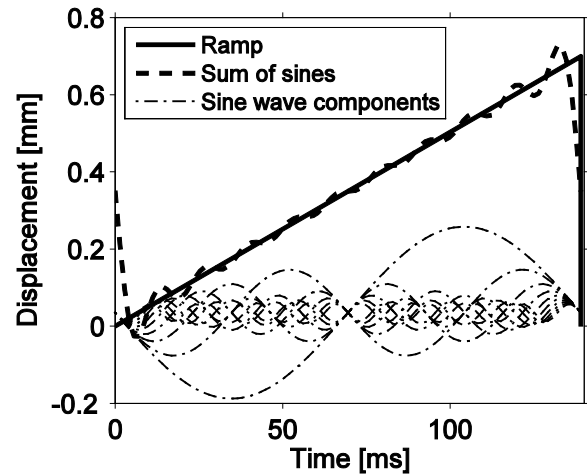


Fig. 18. Decomposition of ramp into sine-wave components for comparison of cyclic test data to dynamic compression tests.

limit below which the only stiffness component that is active is E_∞ . The elastic modulus estimated from the compression tests is used as E_∞ in this paper.

Large material loss at low frequency end

The lumped mass model indicates a much stiffer response than the modulus measured in dynamic compression tests, even in the low frequency end (~ 1 kHz). This stiffness is at an average 316 ± 148 % of the long term structural stiffness. This indicates the presence of significant material loss at frequencies between 100 and 1000 Hz. When compared to material loss parameters reported by previous investigators, the composite skull cores do not exhibit significantly larger loss than pure cortical bone (compiled in reference [9]; shown in Fig. 19) due to the wide confidence intervals. This is an indication that that presence of pores may not influence viscoelasticity of bone in the frequency range under consideration.

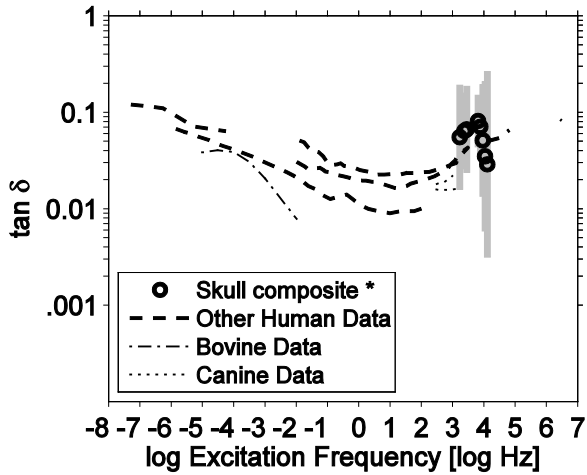


Fig. 19. Skull composite $\tan \delta$ (expected values: circles; 95 % CI: shaded area) as a function of frequency compared to pure cortical bone; data taken from reference [9]

Limitations

Calculated complex modulus tends to diverge to extremely large values at frequencies over 20 kHz. These values are not included in this paper. Divergence may indicate that the frequency domain model assumptions are invalid at frequencies greater than 20 kHz. Also, the long term modulus E_∞ used in this paper comes from dynamic tests and represent the upper limit of quasi-static elastic modulus. Therefore this model will not be able to accurately predict material response to quasi-static rates and will show a stiffer response. This model is valid only for rates of more than 100 Hz.

The influence of potting material on the structural response has not been fully addressed. The entire sample including the potting material is considered to be a homogeneous continuum in this analysis. At an average the combined thickness of the polyester layers is 0.11 mm (~ 15 % of total thickness). From tests conducted on polyester cores, it has been observed that they exhibit a similar response as skull bone ([8]).

The non-linearity of the response to strain level is not discussed. The peak strain in the tests ranged from 43 to 103 μ strain (95 % CI).and peak stress ranged from 53 to 229 kPa.

V. CONCLUSIONS

Effective material loss tangent for skull bone lies between 0.027 and 0.194. While the exact specimen specific loss tangent may not be immediately reportable due to large specimen to specimen variability, these reported average values for the loss tangent can be implemented in current skull FE models to understand how a blast wave changes as it crosses through the skull and into the brain. Previous skull models have had limited skull properties and mesh refinement to even approximate the effect of skull on blast waves. This had led to the over-prediction of pressures and strains inside the brain, and may have led some researchers to over-emphasize the importance of strain in blast related TBI. Combining these viscoelastic skull properties with improved

viscoelastic brain properties may lead researchers to new ideas and injury mechanisms for TBI.

VI. ACKNOWLEDGEMENT

This research was sponsored by contract no. N00421-11-C-0004 from the U.S. Naval Air Warfare Center, Aircraft Division, Patuxent River, MD.

VII. REFERENCES

- [1] Park H C, Lakes R S. Cosserat Micromechanics of Human Bone: Strain Redistribution by a Hydration-Sensitive Constituent. *J Biomechanics*, 1986, 19:385-397.
- [2] Lakes R S, Katz J L, Sternstein S S. Viscoelastic Properties of Wet Cortical Bone: Part I, Torsional and Biaxial studies. *J Biomechanics*, 1979, 12:657-678.
- [3] Garner E, Lakes R S, Lee T, Swan C, Brand R. Viscoelastic Dissipation in Compact Bone: Implications of Stress-Induced Fluid Flow in Bone. *J Biomech Eng*, 2000, 122:166-172.
- [4] Lakes R S. Dynamical Study of Couple Stress Effects in Human Compact Bone, *J Biomech Eng*, 1982, 104:6-11.
- [5] Adler L, Cook C V. Ultrasonic Parameters of Freshly Frozen Dog Tibia. *J Acoust Soc Am*, 1975, 58:1107-1108.
- [6] Thompson G. Experimental Studies of Lateral and Torsional Vibration of Intact Dog Radii. *PhD thesis*, Biomedical Engineering, Stanford University, 1971.
- [7] Soussou J E, Moavenzadeh F, Gradowczyk M H. Application of prony series to linear viscoelasticity. *Transactions of the Society of Rheology*, 1970, 14.4: 573-584.
- [8] Boruah S, Henderson K, Subit D, Salzar R, Shender B, Paskoff G. Response of Human Skull Bone to Dynamic Compressive Loading. *Proceedings of IRCOB Conference*, 2013, Gothenburg.
- [9] Lakes R S. Viscoelastic Properties of Cortical Bone, *Prentice Hall*, Englewood Cliffs, NJ, U.S.A, 2001.

VIII. APPENDIX

TABLE A I
CORE MATERIAL PROPERTIES

Subject	Location	tan δ	E_{∞} [MPa]	Frequency [Hz]				
				100	1000	5000	10000	50000
1	5	0.0667	544	1	70	70	30	50
1	6	0.1715	470	1330	0	220	160	60
1	4	0.0570	365	1305	35	50	50	40
1	2	0.0884	387	833	85	70	160	50
1	3	0.0542	798	1312	20	127	127	20
1	8	0.0233	358	1312	55	40	140	20
2	8	0.0970	541	1389	130	240	133	293
2	6	0.0422	501	1689	15	40	80	250
2	4	0.0491	485	1585	35	90	90	80
2	5	0.0645	327	336	15	56	104	128
2	9	0.1042	384	929	62	50	60	10
2	10	0.0261	616	1724	0	80	120	400
2	3	0.0830	641	1109	45	130	70	60
2	2	0.0865	360	1330	25	190	40	170
2	1	0.0842	438	408	28	30	280	40
3	1	0.0481	633	1701	57	60	300	80
3	2	0.0506	429	2091	110	120	120	140
3	3	0.0466	535	1835	25	40	210	90
3	4	0.0833	523	1487	77	173	133	53
3	5	0.0451	321	1272	10	133	20	20
3	6	0.1052	393	1134	43	127	187	40
3	7	0.0431	336	1774	47	67	53	93
3	8	0.0444	347	1743	45	68	127	7
3	10	0.0810	556	1234	15	170	110	10
4	8	0.0724	556	1271	83	160	200	60
4	7	0.1969	364	351	35	127	253	80
4	6	0.1041	408	732	45	140	40	60
4	4	0.2255	402	808	60	200	100	140
4	5	0.0760	265	1245	55	110	100	50
4	9	0.0658	281	1005	48	90	100	50
4	10	0.1028	341	1012	82	120	140	40
4	3	0.1134	615	302	33	213	180	47
4	2	0.1312	379	611	100	140	80	80
5	8	0.0918	457	1603	80	120	320	160
5	7	0.0976	512	888	70	200	80	60
5	6	0.1184	424	289	372	180	160	70
5	4	0.0474	432	1918	25	80	100	160
5	5	0.0809	363	1687	50	27	213	67
5	9	0.1324	490	860	325	120	160	70
5	10	0.0614	555	1825	120	120	120	360
5	3	0.1035	367	1343	15	220	70	90
5	2	0.0487	391	99	4	60	16	12
5	1	0.0471	352	1678	25	120	130	30
6	8	0.0794	391	1459	63	187	120	40
6	6	0.0422	363	1917	70	100	180	200

Subject	Location	tan δ	E _∞ [MPa]	Frequency [Hz]				
				100	1000	5000	10000	50000
6	4	0.0384	405	2125	45	140	150	40
6	5	0.0283	312	1268	37	100	27	27
6	9	0.0544	270	1440	35	40	110	40
6	3	0.0773	439	1431	15	80	90	90
6	2	0.1370	289	566	15	167	33	60
7	8	0.2160	295	13	165	86	6	10
7	7	0.0932	204	1110	52	140	130	60
7	6	0.0695	305	1585	35	180	80	20
7	4	0.1990	338	107	280	190	170	50
7	5	0.0664	457	1833	45	60	210	10
7	9	0.0805	440	1430	70	213	187	40
7	10	0.1294	363	804	298	380	40	40
7	3	0.1204	514	1099	397	260	320	320
7	2	0.0963	495	1758	277	160	140	60
7	1	0.0906	450	1100	335	70	200	40
8	8	0.0813	211	995	208	110	130	70
8	6	0.1200	546	709	50	230	150	40
8	4	0.0532	395	2035	25	150	70	60
8	5	0.0362	501	1929	35	150	270	20
8	9	0.0715	712	1138	75	130	130	40
8	10	0.0532	519	1791	25	220	70	50
8	3	0.0325	498	1592	20	113	40	27
8	2	0.0543	408	2022	95	170	50	10
8	1	0.0959	530	1420	5	200	210	40
9	4	0.0468	716	2257	92	100	230	90
9	5	0.0346	531	1819	65	120	140	60
9	6	0.0551	434	2096	105	110	240	0
9	7	0.0545	428	2226	197	180	60	60
9	8	0.0390	912	2628	30	140	200	120
9	9	0.0411	656	1997	97	180	100	20
9	10	0.0454	797	2176	73	133	240	40
10	8	0.0975	225	1485	45	40	300	30
10	5	0.1192	291	915	208	210	120	40
10	4	0.0593	586	1624	65	240	60	70
10	9	0.0549	409	1361	85	100	120	40
10	10	0.0538	535	1495	45	60	190	30
10	2	0.0628	418	2102	170	120	300	60
10	1	0.0786	348	1002	100	180	60	40